Supporting Information

Kim et al. 10.1073/pnas.1005828107

SI Text

Device Assembly Example. Fabricated microtip stamps using the design schemes illustrated in Fig. S1*A* exhibited large adhesion differences when characterized via systematic tests using the setup described in Fig. S2*A*. This difference is due primarily to the large contact area reduction between the adhesion "on" and "off" states (Fig. S3*A*). In addition, to demonstrate a device assembly example, we built an unusual class of transistor that combines a printed gate electrode, an air gap dielectric, and a parallel array of single walled carbon nanotubes. Fig. S4*A* shows such a device, with a 100 nm thick air gap dielectric and a gate electrode that consists of a heavily doped ($\rho = 0.0014\ \Omega$cm) silicon platelet (3 μm thick; 100×100 μm), delivered to the device structure by printing. Strategically located patterns of thin metal films provide support structures at the corners of the platelet to define its physical separation from the nanotubes (i.e., the thickness of the air gap dielectric). After growing aligned single walled carbon nanotubes (SWNTs) by chemical vapor deposition (CVD), source and drain electrodes were defined by electron-beam evaporation with 1 nm thick titanium, Ti, and 49 nm thick palladium, Pd, followed by consecutive lift off process in acetone. A peripheral area of SWNT was removed with oxygen reactive ion etching to yield electrically isolated devices. An air gap spacer with 100 nm thick gold was made by electron-beam evaporation and lift off process. A heavily doped ($\rho = 0.0014\ \Omega$cm) silicon platelet was transfer printed on a patterned poly(dimethylsiloxane) (PDMS) surface and then the residue of photoresist anchors was removed with acetone. Finally, the cleaned platelet was transfer printed from the PDMS surface to the air gap spacer and annealing process was performed on a hot plate at 200 °C for 30 min in ambient argon.

The variation in source/drain current (I_{DS}) as a function of gate voltage (V_{GS}) at a source/drain bias (V_{DS}) of −0.05 V for a representative device with channel length and width of 5 μm and 30 μm, respectively, (Fig. S4*B*) appears in Fig. S4*C*. Gate leakage currents less than 10 picoamps, pA, were observed at V_{GS} up to 7 V, where the field strength is somewhat larger than 2 megavolts per centimeter, MV/cm. Increased currents occur for higher voltages, somewhat lower than those expected based on air breakdown according to Pashen's law (1). Accurate models of the capacitance coupling (2) of the gate to the array of tubes (densities of ∼0.5 tubes/μm) can be used together with the measured properties in Fig. S4*C* to estimate the mobility; the result is ∼1,500 cm^2/Vsec, comparable to values reported for related devices with conventional layouts (3). We envision that the type of device presented here could be useful in applications, such as sensing in gases or liquids (4), where both gate modulation and physical access to the nanotubes are required.

Contact Radius at Zero Preload. The shape of microtips can be represented by a spherical portion near the tip and a conical portion in the cylindrical coordinates (r, z),

$$z = f(r) = \begin{cases} R_{\text{microtip}} - \sqrt{R_{\text{microtip}}^2 - r^2} & 0 \le r \le R_{\text{microtip}} \cos\frac{\theta}{2} \\ \frac{r}{\tan\frac{\theta}{2}} - R_{\text{microtip}}\left(\frac{1}{\sin\frac{\theta}{2}} - 1\right) & r > R_{\text{microtip}} \cos\frac{\theta}{2} \end{cases}. \quad \textbf{[S1]}$$

The contact mechanics model (5) relates the radius of contact R_{contact} to the above shape function $f(r)$, work of adhesion γ, and plane-strain modulus $\tilde{E}$ by

$$\frac{\tilde{E} R_{\text{contact}}}{2\pi}\left[\frac{\delta}{R_{\text{contact}}} - \int_0^{R_{\text{contact}}} \frac{f'(r)dr}{\sqrt{R_{\text{contact}}^2 - r^2}}\right]^2 = \gamma, \quad \textbf{[S2]}$$

where δ is related to the preload P by

$$P = 2\tilde{E}\int_0^{R_{\text{contact}}}\left[\delta - t\int_0^t \frac{f'(r)dr}{\sqrt{t^2 - r^2}}\right]dt. \quad \textbf{[S3]}$$

For zero preload $P = 0$, δ is given by

$$\delta = \frac{1}{R_{\text{contact}}}\int_0^{R_{\text{contact}}} \sqrt{R_{\text{contact}}^2 - r^2} f'(r)dr. \quad \textbf{[S4]}$$

The substitution of Eq. **S4** into Eq. **S2** gives the equation for R_{contact}

$$\frac{\tilde{E}}{2\pi R_{\text{contact}}^3}\left[\int_0^{R_{\text{contact}}} \frac{r^2 f'(r)dr}{\sqrt{R_{\text{contact}}^2 - r^2}}\right]^2 = \gamma. \quad \textbf{[S5]}$$

For the shape function in Eq. **S1**, Eq. **S5** gives the following equation for the ratio of radii $\eta = \frac{R_{\text{microtip}}}{R_{\text{contact}}}$,

$$\eta - \frac{\cos^{-1}(\eta\cos\frac{\theta}{2})}{\tan\frac{\theta}{2}} - \eta\frac{\sqrt{1-\eta^2\cos^2\frac{\theta}{2}}}{\sin\frac{\theta}{2}} + (1+\eta^2)\ln\frac{\sqrt{1-\eta^2\cos^2\frac{\theta}{2}} + \eta\sin\frac{\theta}{2}}{1+\eta} + 2\sqrt{\eta}\sqrt{\frac{2\pi\gamma}{\tilde{E}R_{\text{microtip}}}} = 0. \quad \textbf{[S6]}$$

Eq. **S6** gives the implicit expression in Eq. **1**. The contact radius, normalized by $\frac{\gamma}{\tilde{E}}$, is shown in Fig. S5*A*, and so is R_{contact} for material properties in the experiment. For $R_{\text{microtip}} \to 0$, it gives analytically the asymptote in Eq. **2**.

Eq. **S6** holds only when the contact between the microtips and platelet has reached the conical portion. Eq. **S6** requires small microtip radius of curvature,

$$\frac{\tilde{E}R_{\text{microtip}}}{\gamma} \le \frac{8\pi\cos^3\frac{\theta}{2}}{\left[(1+\cos^2\frac{\theta}{2})\ln(\tan\frac{\theta}{4}) + \cos\frac{\theta}{2}\right]^2}. \quad \textbf{[S7]}$$

For microtip radius of curvature exceeding this critical value, the contact between the microtips and platelet remains in the spherical portion, and the corresponding contact radius has been obtained analytically (5). The conical and spherical contacts are also clearly shown in Fig. S5*A*.

Finite Element Analysis of Contact Radius. The contact radii in Eqs. **1** and **2** are derived from classical models of contact mechanics (5), originally developed for the case of a rigid indenter in contact with a soft material. Similar models can be applied to soft indenters in contact with hard materials. For example, Lim and Chaudhri (6) measured the indentation load-displacement curve for a conical indenter of soft rubber in contact with a hard, soda-lime glass. The Young's moduli of rubber (2.45 MPa) and glass (70 GPa) are comparable to those of PDMS (1.8 MPa) and silicon (130 GPa), respectively, reported in main text. The conical indenter, which had the cone angle 60 degree, maximum radius 5 mm,

and round tip radius 0.23 mm, respectively, was used in Lim and Chaudhri's experiments (6).

We studied this axisymmetric indentation problem using the finite element method (FEM), which accounts for the geometric nonlinearity (large change of indenter shape) during indentation. The Poisson's ratio of indenter was 0.4999999 in FEM. We used axisymmetric elements for the rubber indenter, including the detailed geometry of the indenter tip. The element size was ~0.0345 mm, which is 7 times smaller than the indenter tip radius, and 150 times smaller than the maximum indenter radius. Refined meshes were used to ensure that the numerical results converge. The contact between the rubber indenter and the glass expands from an initial cone tip to a conical region as the indentation load increases. The finite sliding, hard contact model in ABAQUS (7) was used, to allow for the possibility of sliding between contact surfaces without interpenetration. The normal and shear stress were continuous within the contact process zone. The friction at the contact interface was also accounted for, but it had negligible effect on the indentation load-displacement: the difference between frictionless contact and contact with a large friction coefficient was less than 0.2%. The results of the indentation load vs. displacement (Fig. S7*A*) indicate excellent agreement between FEM and experiments. This outcome validates the use of FEM for a soft indenter in contact with a hard material.

The same FEM techniques were used to model the experimental configuration in the main text. The pyramid microtips, which had the maximum height 10.6 mm, tip radius 100 nm and cone angle 90 degrees between two opposite edges, respectively, was used in the experiments. The Poisson's ratio of microtip is 0.48. Silicon served as the contacting substrate. The element size was ~1.5 nm, which is 70 times smaller than the indenter tip radius, and 7,000 times smaller than the maximum height of microtip. Fig. S7*B* shows the resulting force vs. displacement curve on each microtip, and a comparison to the contact mechanics model (with cone angle 90°) (5) specified in Eqs. **S2** and **S3**, in which P and δ represent the indentation load and displacement, respectively. The numerical and analytical results agree well at small displacements, but begin to deviate as the displacement increases beyond a couple of microns. The present use of the contact mechanics model (5) involves the determination of contact area in the limit of extremely small displacements, associated with zero imposed compressive load. The results in Fig. S7 indicate that the model (5) is applicable in this regime.

A more direct validation of the contact mechanics model (5) is to use FEM to determine the contact radius for the experimental system. To accomplish this goal, we compressed the microtips into contact with the silicon, and then released the load completely, which delaminates the microtip/platelet interface, as simulated by the Cohesive Behavior Model in ABAQUS (7), with a work of adhesion $\gamma = 155$ mJ/m^2, which is consistent with the value reported in the main text. FEM gives a contact radius of 732 nm, which is slightly larger than 680 nm obtained from Eq. **2** based on the contact mechanics model (5). Both values, however, agree, to within experimental uncertainties (~100 nm), with that determined from analysis of SEM images (i.e., 750 nm). Fig. 2*C* (bottom right frame) shows the deformed FEM mesh of final contact (in this zero compressive load regime).

Minimum Height of Microtips. Similar to (8), the minimum height corresponds to the critical state of vanishing preload at which the elastic energy in the stamp due to the collapse of the post equals the adhesion energy between the stamp and platelet. The latter equals the product of work of adhesion γ and contact area, while the former can be obtained using an approach based on fracture mechanics (8), which accounts for the finite geometry of the stamp, such as the stamp width w_{stamp} and contact radius R_{contact} between the microtips and platelet. The contact area is determined analytically by minimizing the total potential energy, which equals the elastic energy in the stamp subtracted by the adhesion energy. The minimum height of microtips is then obtained analytically as

$$h_{\min} = \sqrt{\frac{w_{\text{stamp}}\gamma}{\bar{E}}\left[3.04\ln\left(\frac{w_{\text{stamp}}}{R_{\text{contact}}}\right) - 4.44\right]}, \qquad \textbf{[S8]}$$

where the factors 3.04 and 4.44 result from the stress intensity factor for finite geometry in fracture mechanics. The substitution of the asymptote in Eq. **2** for R_{contact} leads to the analytical expression in Eq. **3**.

Fig. S5*B* shows the minimum height of microtips, normalized by post width w_{stamp}, increases with the work of adhesion γ but decreases with the plane-strain modulus of the stamp. The minimum height for the material properties and post width in experiments is also shown. The experimental data for delamination (above the curve) and collapse (on or below the curve) agree well with the model.

Analysis of Stamp Collapse Process. For the microtip height larger than $h_{\min}$ in Eq. **3**, the process of stamp collapse consists of four stages as the preload P increases; (*i*) microtip contact, during which only microtips contact the platelet; (*ii*) post collapse, which corresponds to a sudden increase of contact area between the post and platelet; (*iii*) post contact, during which the contact area remains the same as the preload increases; and (*iv*) zipping of interface, which corresponds to the increase of contact area with the preload.

i. microtip contact: The deformation in the microtips and post is studied by linear elasticity, where the microtips are subject to uniaxial compression, and the post is subject to the preload and reaction forces from the microtips.
ii. post collapse: The analysis is similar to that for the minimum height, except that the total potential energy includes the external work of the preload. Analytical model gives the following three equations to determine the ratio c_{collapse} of contact area to stamp area at collapse, the corresponding critical load P_{collapse}, and the compressed height h_{collapse} of microtips at collapse,

$$\frac{1}{F_1(b)}\left(\frac{h_{\text{collapse}}}{w_{\text{stamp}}}\right)^2 \frac{K\left(\frac{c_{\text{collapse}}}{b}\right)}{K\left[\sqrt{1-\left(\frac{c_{\text{collapse}}}{b}\right)^2}\right]} - \frac{h_{\text{collapse}}}{w_{\text{stamp}}}\frac{P_{\text{collapse}}}{w_{\text{stamp}}^2\bar{E}}\left[c_{\text{collapse}}\right.$$
$$\left.+\left(\sqrt{2bc_{\text{collapse}}+2c_{\text{collapse}}^2}-2c_{\text{collapse}}\right)F_2(b-c_{\text{collapse}})\right]$$
$$+\frac{3h_{\text{microtip}}}{4w_{\text{stamp}}}(1-b)\left(\ln\frac{h_{\text{collapse}}}{h_{\text{microtip}}}\right)^2 - \frac{4h_{\text{microtip}}}{3w_{\text{stamp}}}\frac{1}{1-b}\left(\frac{P_{\text{collapse}}}{w_{\text{stamp}}^2\bar{E}}\right)^2$$
$$-\frac{2\gamma}{w_{\text{stamp}}\bar{E}}c_{\text{collapse}} = 0, \qquad \textbf{[S9]}$$

$$\frac{1}{F_1(b)}\left(\frac{h_{\text{collapse}}}{w_{\text{stamp}}}\right)^2 \frac{d}{dc}\left\{\frac{K(c/b)}{K[\sqrt{1-(c/b)^2}]}\right\}\Bigg|_{c=c_{\text{collapse}}} - \frac{h_{\text{collapse}}}{w_{\text{stamp}}}\frac{P_{\text{collapse}}}{w_{\text{stamp}}^2\bar{E}}$$
$$\times\left[1+\left(\frac{b+2c_{\text{collapse}}}{\sqrt{2bc_{\text{collapse}}+2c_{\text{collapse}}^2}}-2\right)F_2(b-c_{\text{collapse}})\right.$$
$$\left.-\left(\sqrt{2bc_{\text{collapse}}+2c_{\text{collapse}}^2}-2c_{\text{collapse}}\right)F_2'(b-c_{\text{collapse}})\right]$$
$$-\frac{2\gamma}{w_{\text{stamp}}\bar{E}} = 0, \qquad \textbf{[S10]}$$

$$\frac{1}{F_1(b)}\frac{h_{\text{collapse}}^2}{w_{\text{stamp}}h_{\text{microtip}}}\frac{K(\frac{c_{\text{collapse}}}{b})}{K[\sqrt{1-(\frac{c_{\text{collapse}}}{b})^2}]}+\frac{3(1-b)}{4}\ln\frac{h_{\text{collapse}}}{h_{\text{microtip}}}$$
$$-\frac{h_{\text{collapse}}}{h_{\text{microtip}}}\frac{P_{\text{collapse}}}{w_{\text{stamp}}^2\bar{E}}[F_2(b-c_{\text{collapse}})(\sqrt{2bc_{\text{collapse}}+2c_{\text{collapse}}^2}$$
$$-2c_{\text{collapse}})-1+c_{\text{collapse}}]=0, \quad \textbf{[S11]}$$

where $b=1-\frac{4w_{\text{microtip}}^2}{3w_{\text{stamp}}^2}$, $K(k)=\int_0^{\pi/2}\frac{d\varphi}{\sqrt{1-k^2\sin^2\varphi}}$ is the elliptical function of the first kind, $F_1(k)=-0.417-1.07\ln(1-k)$, and $F_2(k)=(1-0.25k+0.093k^2-0.005k^3)/\sqrt{1-0.5k}$.

iii. post contact: The contact area is the same as that in (*ii*), but the energy release rate at the boundary of contact decreases as the preload increases. The compressed height h' of microtips decreases with the increase of preload, and is given by

$$\frac{1}{F_1(b)}\frac{h'^2}{w_{\text{stamp}}h_{\text{microtip}}}\frac{K(\frac{c_{\text{collapse}}}{b})}{K[\sqrt{1-(\frac{c_{\text{collapse}}}{b})^2}]}+\frac{3(1-b)}{4}\ln\frac{h'}{h_{\text{microtip}}}$$
$$-\frac{h'}{h_{\text{microtip}}}\frac{P}{w_{\text{stamp}}^2\bar{E}}[F_2(b-c_{\text{collapse}})(\sqrt{2bc_{\text{collapse}}+2c_{\text{collapse}}^2}$$
$$-2c_{\text{collapse}})-1+c_{\text{collapse}}]=0. \quad \textbf{[S12]}$$

iv. zipping of interface: The energy release rate at the boundary of contact reaches and remains at zero, and the contact area increases with the preload. The ratio c of contact area to stamp area increases with the preload, while the opposite holds for the compressed height h' of microtips, and they are given by

$$\frac{1}{F_1(b)}\frac{h'^2}{w_{\text{stamp}}h_{\text{microtip}}}\frac{K(\frac{c}{b})}{K[\sqrt{1-(\frac{c}{b})^2}]}+\frac{3(1-b)}{4}\ln\frac{h'}{h_{\text{microtip}}}$$
$$-\frac{h'}{h_{\text{microtip}}}\frac{P}{w_{\text{stamp}}^2\bar{E}}[F_2(b-c)(\sqrt{2bc+2c^2}-2c)-1+c]=0, \quad \textbf{[S13]}$$

$$h'=F_1(b)\frac{P}{w_{\text{stamp}}\bar{E}}\left(1-\frac{c}{b}\right)\sqrt{\frac{c}{2}(b+c)}K\left[\sqrt{1-\left(\frac{c}{b}\right)^2}\right]F_2(b-c). \quad \textbf{[S14]}$$

This analysis gives the following slope change in the preload-distance curve (Fig. 3*A*), maximum height of microtips, and restoring force in microtips.

Slope Change in the Preload-Distance Curve. The distance in Fig. 3*A* before post collapse consists of the (compressive) displacements in microtips and in the post. The microtips are subject to uniaxial compression, while the post is modeled as a semiinfinite solid subject to remote compression and forces from the microtips on the surface. The ratio of preload to this distance gives the slope k_{microtip}

$$\frac{1}{k_{\text{microtip}}}=\frac{1}{w_{\text{microtip}}E}\left[\frac{3h_{\text{microtip}}}{4w_{\text{microtip}}}+\frac{1}{\pi}\left(\frac{w_{\text{microtip}}}{w_{\text{stamp}}}-\frac{2w_{\text{microtip}}^3}{w_{\text{stamp}}^3}\right)\ln\left(\frac{w_{\text{stamp}}^2}{2w_{\text{microtip}}^2}-1\right)\right]+\frac{h_{\text{stamp}}}{w_{\text{stamp}}^2E}, \quad \textbf{[S15]}$$

where h_{stamp} is the effective height of the stamp (Fig. S1*A*).

The change of distance in Fig. 3*A* after post collapse also consists of contributions from the microtips and from the post, but the former becomes negligible as compared to the latter. The ratio of preload increment to distance increment gives the slope k_{post}

$$\frac{1}{k_{\text{post}}}=\frac{h_{\text{stamp}}}{w_{\text{stamp}}^2E}. \quad \textbf{[S16]}$$

Eqs. **S15** and **S16** lead to Eq. **5**.

Restoring Force in Microtips. The restoring force microtips is given by

$$F=P[(\sqrt{2bc+2c^2}-2c)F_2(b-c)-1+c]-\frac{w_{\text{stamp}}\bar{E}}{F_1(b)}\frac{K(\frac{c}{b})}{K(\sqrt{1-\frac{c^2}{b^2}})}h', \quad \textbf{[S17]}$$

where c and h' are determined from Eqs. **S9** to **S14** for stages (*ii*)–(*iv*).

Maximum Height of Microtips. The maximum height of microtips is determined by equating the energy release rate to the work of adhesion, which gives the following relation to determine c

$$\frac{\pi P^2}{4w_{\text{stamp}}^3\bar{E}}(b-c)[F_2(b-c)]^2=\gamma. \quad \textbf{[S18]}$$

Eq. **S14** then gives explicitly h'. The maximum height of microtips, $h_{\max}$, is then obtained from Eq. **S13** by replacing h_{microtip} with $h_{\max}$.

Fig. S5*C* shows the maximum height of microtips, normalized by post width w_{stamp}, increases with the preload as well as the work of adhesion γ but decreases with the plane-strain modulus of the stamp. The maximum height for the material properties and post width in experiments is also shown. The experimental data for retrieval (below the curve) and failure (above the curve) agree well with the model.

Viscoelastic Analysis. For operation in retrieval mode, the PDMS stamp is retracted sufficiently quickly to ensure that the platelet/substrate interface fractures, but the stamp/platelet interface does not, due to effects of viscoelastic behavior in the PDMS. The creep compliance of PDMS, is an important material property that governs this process. This quantity, as measured by Xu et al. (9), can be represented by a piece-wise relation

$$\frac{C(t)}{C(\infty)}=\begin{cases}0.198\times[6.14+\log(t)] & 0.0001<t<0.08\\ 1 & 0.08<t\end{cases}, \quad \textbf{[S19]}$$

which is a nondecreasing function of time t (unit: second). The viscoelastic energy release rate G is related to the stress intensity factor $K(t)$ via the creep compliance by (10)

$$G=\frac{1}{2\bar{E}}\frac{C(t)}{C(\infty)}K^2(t), \quad \textbf{[S20]}$$

where $\bar{E}$ is the plane-strain modulus of PDMS, and the factor $1/2$ accounts for the elastic mismatch between PDMS and silicon (8). The stress intensity factor $K(t)$ is given by

$$K_I=\frac{\bar{E}h''}{F_1(b)}\sqrt{\frac{\pi}{2w_{\text{stamp}}c[1-(\frac{c}{b})^2]}}\frac{1}{K[\sqrt{1-(\frac{c}{b})^2}]}$$
$$+\frac{P''}{2w_{\text{stamp}}}\sqrt{\frac{\pi(b-c)}{w_{\text{stamp}}}}F_2(b-c), \quad \textbf{[S21]}$$

where w_{stamp} is the stamp width, b and functions F_1, F_2, and K are defined after Eq. **S11**, c is solved from Eqs. **S13** and **S14**, P'' is the pull-off force, and the microtip height h'' is related to P'' by

$$\frac{1}{F_1(b)}\frac{h''^2}{w_{\text{stamp}}h_{\text{microtip}}}\frac{K(\frac{c}{b})}{K[\sqrt{1-(\frac{c}{b})^2}]}+\frac{3(1-b)}{4}\ln\frac{h''}{h_{\text{microtip}}}$$
$$+\frac{h''}{h_{\text{microtip}}}\frac{P''}{w_{\text{stamp}}^2\tilde{E}}[F_2(b-c)(\sqrt{2bc+2c^2}-2c)-1+c]=0, \quad \textbf{[S22]}$$

which is identical to Eq. **S13** except that P and h' are replaced by $-P''$ and h'', respectively.

The pull-off force is related to the pulling speed v_{pulling} and time t by

$$P''=w_{\text{stamp}}E(v_{\text{pulling}}t-L_{\text{compression}}), \quad \textbf{[S23]}$$

after the compression force P is relaxed, where $L_{\text{compression}}$ is the compressed distance of the stamp due to P, and $L_{\text{compression}}=20$ μm from Fig. 3*A*.

The stamp/platelet interface will not delaminate if the viscoelastic energy release rate remains smaller than the work of adhesion γ, i.e.,

$$G<\gamma \quad \textbf{[S24]}$$

For the material properties given in the main text, the creep compliance in Eq. **S19**, and pulling speed $v_{\text{pulling}}=460$ μm/s, the above inequality gives a critical time of 0.052 s for the stamp/platelet interface starting to debond. The pull-off force is then obtained from Eq. **S23**.

1. Hourdakis E, Simonds BJ, Zimmerman NM (2006) Submicron gap capacitor for measurement of breakdown voltage in air. *Rev Sci Instrum* 77:034702-1–034702-4.
2. Cao Q, et al. (2007) Gate capacitance coupling of single-walled carbon nanotube thin-film transistors. *Appl Phys Lett* 90:023516-1–023516-3.
3. Zhou X, Park JY, Huang S, Liu J, McEuen PL (2005) Band structure, phonon scattering, and the performance limit of single-walled carbon nanotube transistors. *Phys Rev Lett* 95:146805-1–146805-4.
4. Cao Q, Rogers JA (2009) Ultrathin films of single-walled carbon nanotubes for electronics and sensors: a review of fundamental and applied aspects. *Adv Mater* 21:29–53.
5. Maugis D (1995) Extension of the Johnson-Kendall-Roberts Theory of the elastic contact of spheres to large contact radii. *Langmuir* 11:679–682.
6. Lim YY, Chaudhri MM (2003) Experimental investigations of the normal loading of elastic spherical and conical indenters on to elastic flats. *Philos Mag* 83:3427–3462.
7. Dassault Systèmes (2009) *Abaqus analysis user's manual v.6.9*. (Dassault Systèmes Simulia Corp., Rhode Island).
8. Huang Y, et al. (2005) Stamp collapse in soft lithography. *Langmuir* 21:8058–8068.
9. Xu Z, et al. (2008) Broadband measurement of rate-dependent viscoelasticity at nanoscale using scanning probe microscope: Poly(dimethylsiloxane) example. *Appl Phys Lett* 93:133103.
10. Schapery RA (1975) A theory of crack initiation and growth in viscoelastic media II. Approximate methods of analysis. *Int J Fracture* 11:369–388.

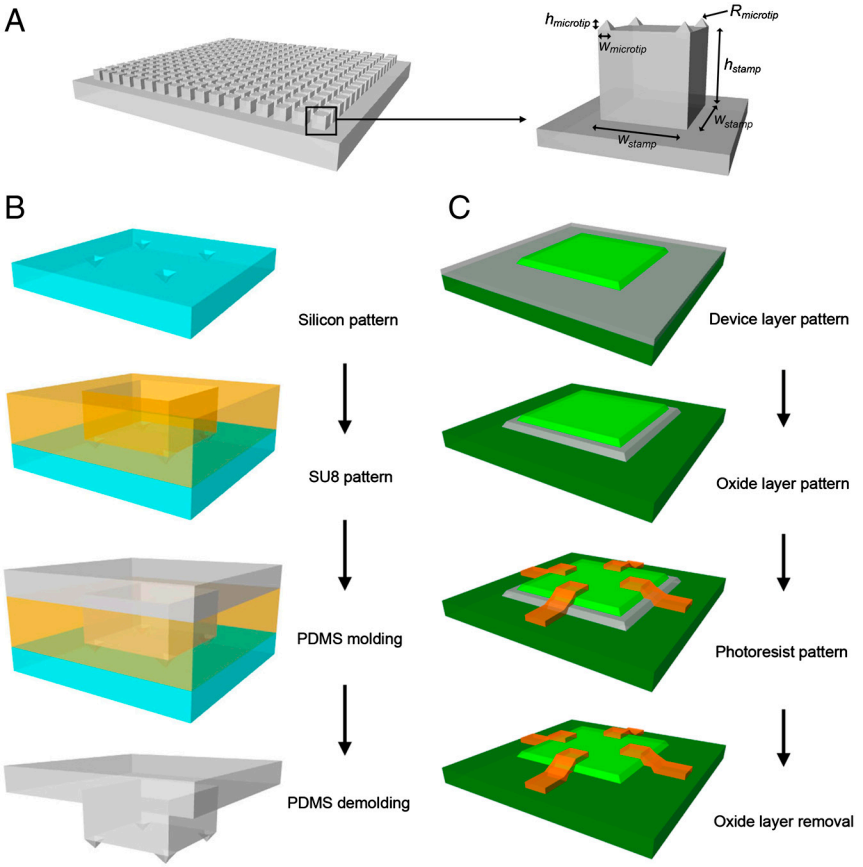

Fig. S1. (*A*) Elastomeric, microtip adhesive surface consisting of four features of pyramidal relief on the surfaces of square posts in a square array. (*B*) Schematic illustration of the process for making microtip stamps of PDMS by casting and curing against a photolithographically defined pattern of SU8 on an anisotropically (KOH) etched silicon (100) wafer. (*C*) Schematic illustration of the process for fabricating silicon platelets in printable configurations, starting with silicon-on-insulator (SOI) wafers with 3 μm or 260 nm thick top Si layers.

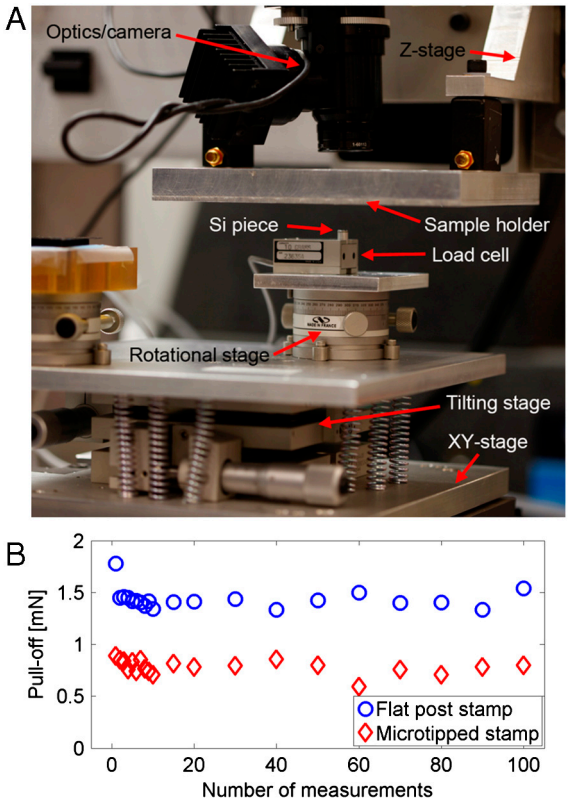

Fig. S2. (*A*) Picture of a custom adhesion testing setup design to measure pull-off forces with elastomeric, microtip stamps. (*B*) Pull-off force data of a stamp with four-tipped layout and a corresponding flat surface measured repeatedly with 200 μm/s retraction speed and 2 mN preload constantly up to 100 times.

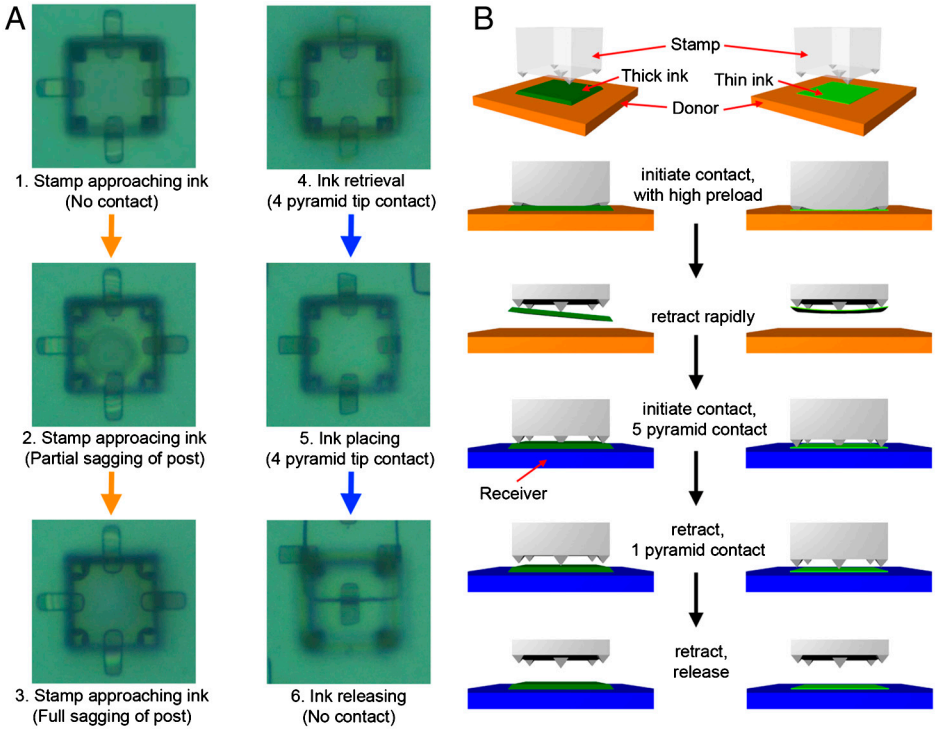

Fig. S3. (*A*) Optical microscope top view images, collected by viewing through a transparent microtip stamp, during various stages of the printing. (*B*) Schematic illustration of the process for transfer printing with a microtip stamp that has a five-tipped design. The largest microtip, located at center, is the only point of contact between the stamp and the ink at the final stage of the transfer process.

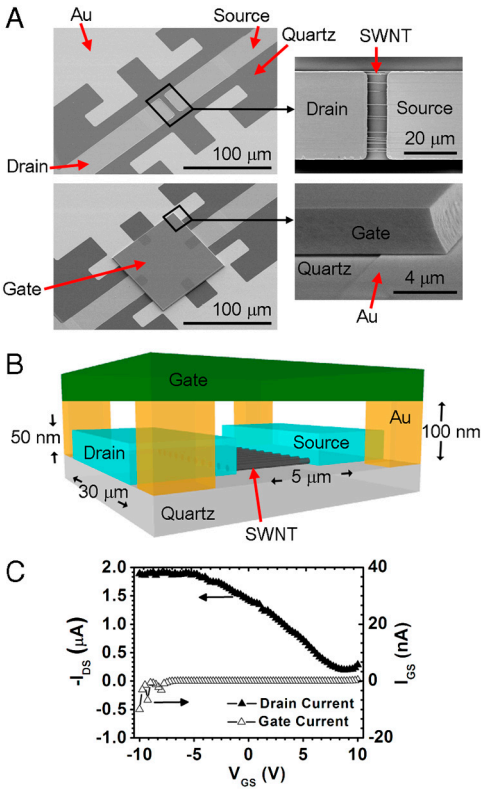

Fig. S4. (*A*) SEM images of carbon nanotube field effect transistor (CNFET) with 100 nm thick air gap dielectric fabricated using transfer printing a heavily doped ($\rho = 0.0014\ \Omega$cm) silicon platelet (3 μm thick; 100 × 100 μm). The right frames provide the magnified view of single walled carbon nanotubes (SWNTs) under the silicon platelet and 100 nm air gap between a gate and a quartz substrate in the left frames. (*B*) Schematic illustration of the CNFET with dimensions. (*C*) Transfer characteristics for the CNFET.

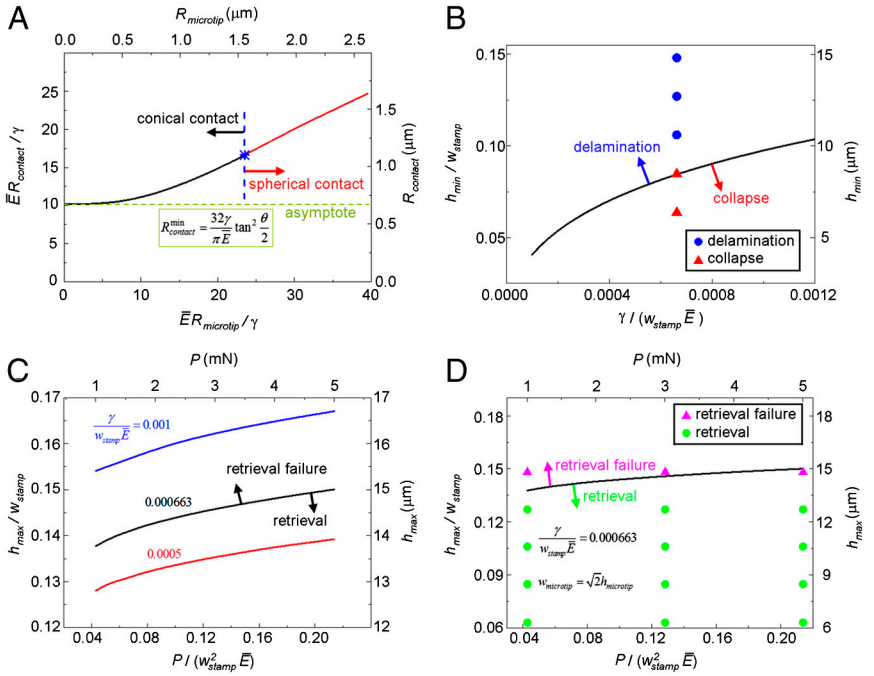

Fig. S5. (*A*) The contact radius (at zero preload) between the microtips and platelet vs. the microtip radius of curvature for the microtip cone angle $\theta = 90°$. The asymptote for vanishing microtip radius gives minimal contact radius. (*B*) The minimum height of microtips vs. the work of adhesion (normalized by the post width and plane-strain modulus of the stamp) for $\theta = 90°$, together with the experimental data for delamination and collapse. (*C*) The maximum height of microtips vs. the preload for several values of work of adhesion. (*D*) The maximum height of microtips vs. the preload, together with the experimental data for retrieval and failure.

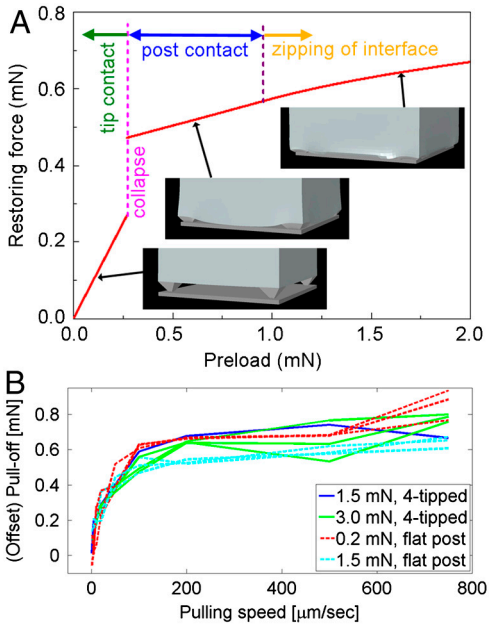

Fig. S6. (*A*) Restoring force associated with compression of microtips on the surface of an elastomer as a function of preload, during loading with corresponding images of finite element modeling results. (*B*) Master plot of force required to separate an elastomer surface from a flat substrate, as a function of retraction speed for different preload cases from Fig. 3*C*, *D*. The data include the cases of elastomeric posts that terminate in flat surfaces and in sets of four microtips, scaled to account for the mechanics of the microtips, according to theoretical modeling.

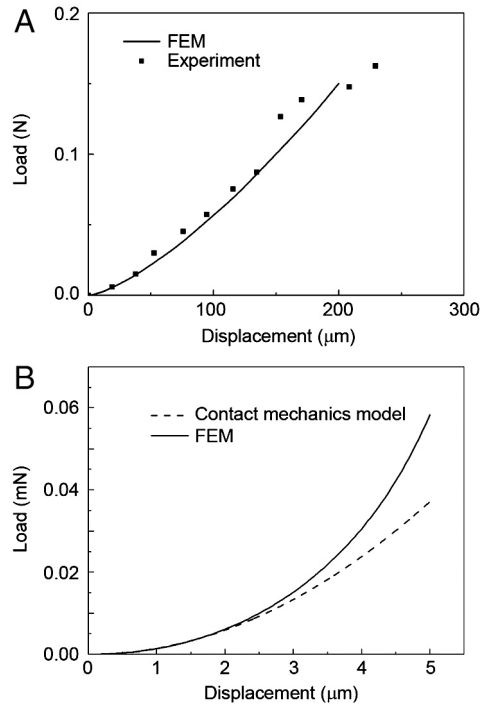

Fig. S7. (*A*) Load-displacement comparison between FEM results and experimental data for the case of the system of Lim and Chaudhri. (*B*) Load-displacement comparison between FEM results and contact mechanics model for a PDMS microtip pressed against a silicon substrate.